3D Gaussian Splatting for Annular Dark Field Scanning Transmission Electron Microscopy Tomography Reconstruction

Supplementary Material

Table 1. Quantitative comparison of Mo–PtNi [3] under 45-view reconstruction.

	Train view		Test view	
Method	PSNR↑	SSIM↑	PSNR↑	SSIM↑
SIRT [5]	27.28	0.703	24.23	0.603
FDK [1]	18.92	0.527	16.71	0.409
GENFIRE [4]	28.97	0.723	27.19	0.653
3D GS [2]	8.93	0.201	8.93	0.201
Ours	**34.14**	**0.897**	**31.72**	**0.835**

Table 2. Quantitative comparison of Mo–PtNi [3] under 15-view reconstruction.

	Train view		Test view	
Method	PSNR↑	SSIM↑	PSNR↑	SSIM↑
SIRT [5]	23.61	0.712	22.15	0.572
FDK [1]	16.01	0.537	15.31	0.402
GENFIRE [4]	26.72	0.739	25.21	0.599
3D GS [2]	8.93	0.201	8.93	0.201
Ours	**32.28**	**0.881**	**28.37**	**0.782**

This supplementary material provides more details and results that are not included in the main paper due to space limitations. The contents are organized as follows:

- Section 1 presents the role of coefficient γ in our method and provides its mathematical derivation.
- Section 2 presents 3D reconstruction results on the Mo–PtNi material, including both qualitative and quantitative comparisons under 45-view and 15-view.
- Section 4 presents the results of ablation on 2D Fourier Loss using Mo–PtNi 3D volume.
- Section 4 presents evaluation metrics, including 3D PSNR, 3D SSIM, and FSC, to validate the volumetric accuracy on real and simulated datasets.
- Section 5 presents the runtime of our method together with the compared methods.
- Section 6 presents the ground-truth and rendered images of all views for both training and testing in the PtNi and Mo–PtNi reconstructions.

1. The Mathematical Derivation of Coefficient Γ

In Annular Dark-Field Scanning Transmission Electron Microscopy (ADF-STEM) tomography, the physical basis of reconstruction is Rutherford elastic scattering. The scattering intensity of the specimen depends solely on the local atomic density and the atomic number Z, being proportional to the denza coefficient $d_i = density \cdot Z^{\alpha}$. This property is intrinsic to the material and independent of the incident angle of the electron beam.

When modeling within the 3D Gaussian Splatting framework, a fundamental contradiction arises. Each 3D Gaussian kernel is represented as an ellipsoidal distribution defined by its covariance matrix Σ_i. As the electron beam is projected along different angles, the effective path length through the kernel varies. Longer paths yield larger uncorrected scattering contributions, while shorter paths yield smaller ones. Consequently, the scattering contribution of the same kernel fluctuates with angle, violating the principle that scattering intensity should be angle-independent. This inconsistency introduces reconstruction artifacts such as missing-wedge effects and structural distortions.

To address this issue, we introduce the Scattering-View-Consistent coefficient γ. Its role is to dynamically compensate for the angle dependence of the path length, ensuring that the scattering contribution of each Gaussian kernel remains invariant with respect to the incident angle.

Each 3D Gaussian kernel is normalized as

$$G_3(\mathbf{x}; \boldsymbol{\mu}_i, \boldsymbol{\Sigma}_i) = \frac{1}{(2\pi)^{3/2}|\boldsymbol{\Sigma}_i|^{1/2}} \times \exp\left(-\frac{1}{2}(\mathbf{x}-\boldsymbol{p}_i)^{\top}\boldsymbol{\Sigma}_i^{-1}(\mathbf{x}-\boldsymbol{p}_i)\right), \quad (1)$$

where p_i is the kernel center, Σ_i is the three-dimensional covariance matrix, and $|\Sigma_i|$ encodes the kernel volume.

For an electron beam projected along a ray R, the uncorrected scattering contribution is given by

$$S_{\text{raw}}(\theta) = d_i \int_R G_3(\mathbf{x})\, d\mathbf{x}, \quad (2)$$

which depends on the projection angle θ. To eliminate this dependence, we require the corrected scattering contribution to be angle-invariant:

$$\gamma_i \cdot S_{\text{raw}}(\theta) = C_i, \quad (3)$$

where C_i is a constant. Thus,

$$\gamma_i \propto 1 \Big/ \int_R G_3(\mathbf{x})\, d\mathbf{x}. \quad (4)$$

Using Gaussian integral identities and orthogonal projection properties, the line integral through the kernel can be expressed as

$$\int_R G_3(\mathbf{x})\, d\mathbf{x} \propto \sqrt{\frac{|\boldsymbol{\Sigma}_i|}{|\boldsymbol{\Sigma}_i^{(2D)}|}}, \quad (5)$$

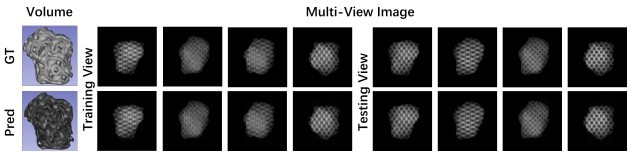

Figure 1. Reconstruction results with 25 views. Comparison of ground truth (3D/2D) and our predictions. Our approach achieves high fidelity in both volumetric and projection domains.

Table 3. Quantitative evaluation on real and simulated datasets. We report odd-even split FSC for the real dataset, and 3D metrics for the 25-view simulated dataset.

Method	**Real Data**	**Simulation**		
	FSC (Å) ↓	3D PSNR ↑	3D SSIM ↑	FSC (Å) ↓
SIRT [1]	8.67	24.15	0.623	8.42
FDK [8]	12.53	18.32	0.410	12.61
GENFIRE [26]	6.34	28.45	0.715	6.23
Ours	**4.24**	**33.82**	**0.912**	**4.15**

where $\Sigma_i^{(2D)}$ is the two-dimensional projected covariance matrix onto the imaging plane.

Substituting into the constraint yields the final formula

$$\gamma_i = \sqrt{\frac{|\mathbf{\Sigma}_i|}{|\mathbf{\Sigma}_i^{(2D)}|}}. \tag{6}$$

$\Sigma_i^{(2D)}$ denotes the determinant of the two-dimensional projected covariance, which varies with angle. By taking this ratio, γ dynamically compensates for angular variations in path length, thereby restoring the physical consistency of scattering contributions.

2. Comparison with Mo-PtNi

Table 1 and Table 2 present the results of comparative experiments on the Mo–PtNi material under 45-view and 15-view settings. Our method outperforms the baselines in both PSNR and SSIM, confirming that the reconstructed 3D volume is structurally the most faithful to the ground truth.

3. Extended Evaluation on Real and Simulated Data

To comprehensively validate the volumetric accuracy of our method against the ground truth, we provide extended evaluation metrics beyond standard 2D projections, including 3D PSNR, 3D SSIM, and Fourier Shell Correlation (FSC).

For the real dataset, we compute the odd-even FSC, achieving an impressive resolution of 4.2 Å. Furthermore, we evaluate our method on simulated datasets using GT-FSC, 3D PSNR, and 3D SSIM to rigorously assess volumetric fidelity.

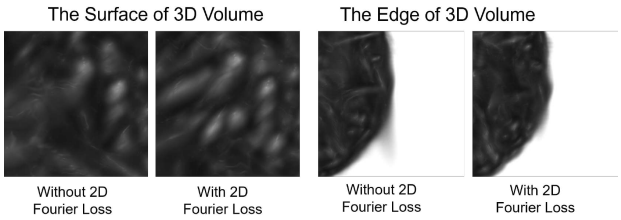

Figure 2. The ablation on 2D Fourier Loss with Mo–PtNi.

As detailed in Table 3, our method significantly outperforms baseline approaches, including SIRT, FDK, and GENFIRE, across all 3D volumetric metrics on both real and simulated datasets. Additionally, Figure 1 provides a visual comparison of the 3D volumes and 2D projections between the ground truth and our reconstruction under a 25-view sparse setting. The results clearly demonstrate that our proposed DenZa-Gaussian method preserves superior structural fidelity and high-frequency details compared to traditional methods.

4. Ablation on 2D Fourier Loss with Mo–PtNi

We conducted the ablation study on the 2D Fourier Loss in the 3D reconstruction of the Mo–PtNi material. Figure 2 shows the surface comparison of the reconstructed 3D volume on the left and the edge comparison on the right. The ablation study confirms that the 2D Fourier Loss contributes to retaining high-frequency details while reducing artifacts, thereby improving edge smoothness.

5. Runtime

In terms of runtime, FDK completes the reconstruction within a few seconds, while SIRT requires several minutes. However, the reconstruction quality of both methods falls short of the demands of scientific research. Compared with these approaches, GENFIRE achieves higher reconstruction quality but requires more than ten hours of computation. By contrast, our method attains the best results in both PSNR and SSIM metrics, while reducing the reconstruction time to only 12 minutes, thereby achieving the optimal balance between efficiency and quality.

6. The Ground-truth and Rendered Images

In Figure 3 and Figure 4, we present ground-truth and rendered images of Mo-PtNi 3D reconstruction for both training and test views under 45-view and 15-view settings. From these figures, it is evident that our reconstructed 3D volume closely approximates the ground truth in both contour and intensity, demonstrating superior reconstruction quality.

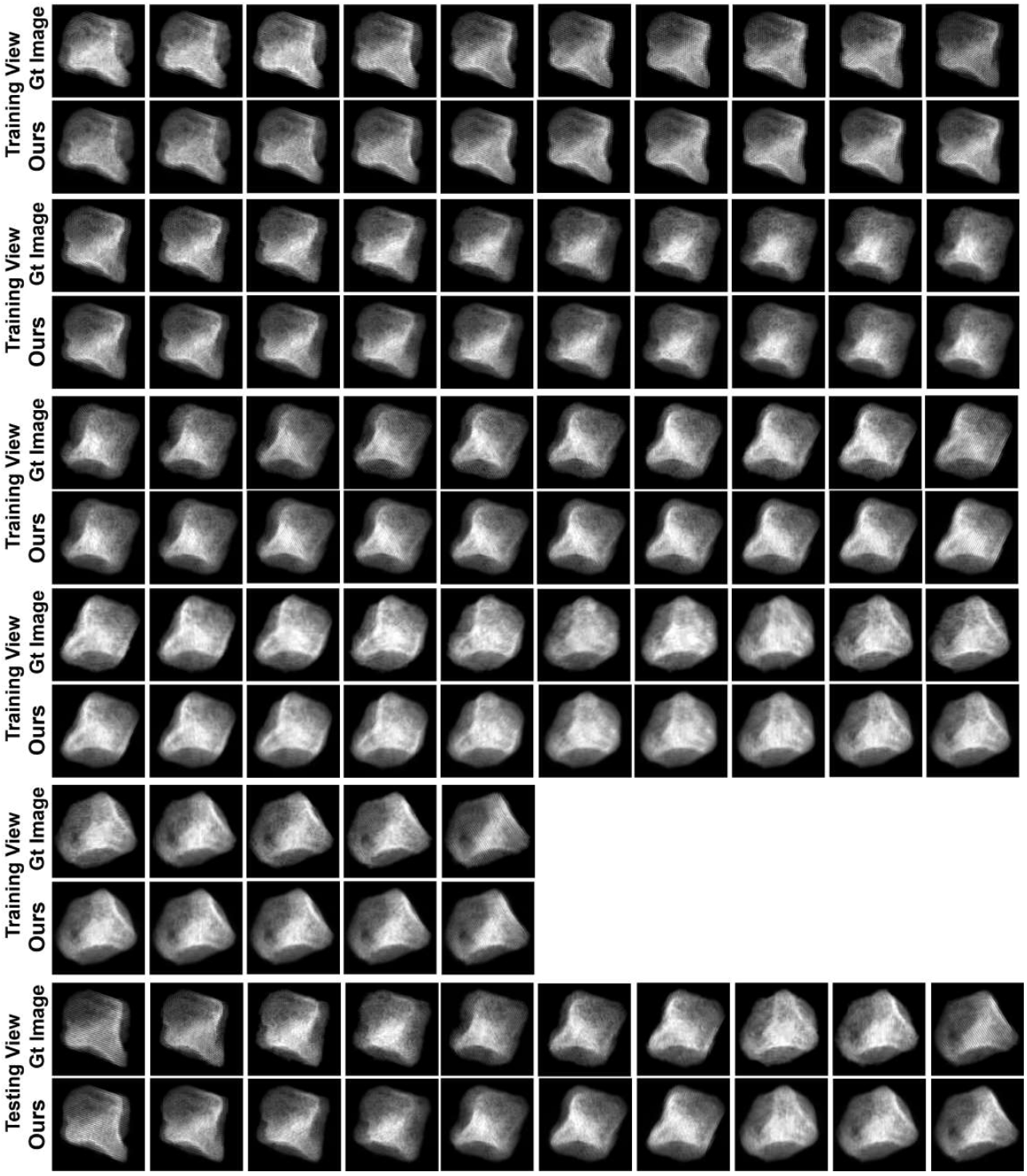

Figure 3. Visualization results of the Mo-PtNi [3] 3D reconstruction under the 45-view setting, including all ground-truth and rendered images for both training and test views.

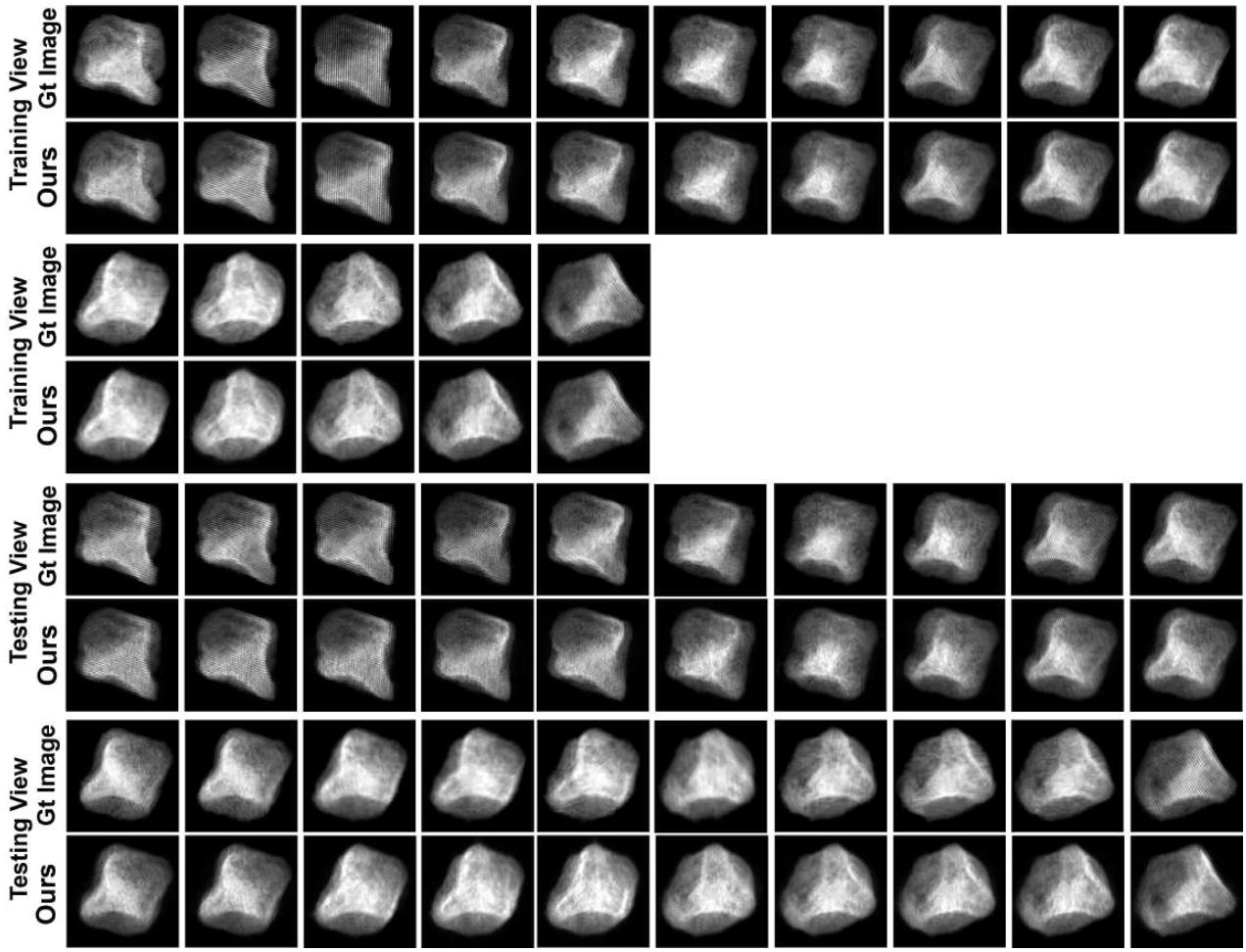

Figure 4. Visualization results of the PtNi [3] 3D reconstruction under the 15-view setting, including all ground-truth and rendered images for both training and test views.

References

[1] Lee A Feldkamp, Lloyd C Davis, and James W Kress. Practical cone-beam algorithm. *Journal of the Optical Society of America A*, 1(6):612–619, 1984. 1

[2] Bernhard Kerbl, Georgios Kopanas, Thomas Leimkühler, and George Drettakis. 3d gaussian splatting for real-time radiance field rendering. *ACM Trans. Graph.*, 42(4):139–1, 2023. 1

[3] Juhyeok Lee, Chaehwa Jeong, and Yongsoo Yang. Single-atom level determination of 3-dimensional surface atomic structure via neural network-assisted atomic electron tomography. *Nature Communications*, 12(1):1962, 2021. 1, 3, 4

[4] Alan Pryor Jr, Yongsoo Yang, Arjun Rana, Marcus Gallagher-Jones, Jihan Zhou, Yuan Hung Lo, Georgian Melinte, Wah Chiu, Jose A Rodriguez, and Jianwei Miao. Genfire: A generalized fourier iterative reconstruction algorithm for high-resolution 3d imaging. *Scientific reports*, 7(1):10409, 2017. 1

[5] Jeannot Trampert and Jean-Jacques Leveque. Simultaneous iterative reconstruction technique: Physical interpretation based on the generalized least squares solution. *Journal of Geophysical Research: Solid Earth*, 95(B8):12553–12559, 1990. 1